VSC-driven Modeling for Soft Open Points and Battery Energy Storage Systems to Balance Three-phase Distribution Networks with Phase-specific Dispatching

Chengwei Lou, Ran Zhao, Hangxing Zhang, Lu Zhang, *Senior Member*, *IEEE*, Wei Tang, *Member*, *IEEE*, Jin Yang, *Member*, *IEEE*, and Linjuan Zhang

***Abstract*—This paper proposes an advanced voltage source converter (VSC)-driven model for soft open points (SOPs) and battery energy storage systems (BESSs) to actively balance three-phase distribution networks. The proposed model addresses the phase imbalance caused by the increasing integration of renewable energy and distributed generation. Unlike traditional models, which mainly focus on AC capacity constraints, the proposed model explores the complexities of the DC-link. This allows for a thorough examination of the interactions between active and reactive power, as well as the voltage levels on both the AC and DC sides of VSCs. The relationship between pulse width modulation (PWM) control configurations and VSC power outputs is discussed, enhancing control on both sides of the converters. This improvement also facilitates better cross-phase power transfer through SOPs and enhances the overall balance among the three phases. In addition, the proposed model incorporates the cooperative functionality of VSC-driven BESSs to sustain the phase balance. To further optimize the load distribution, phase-specific dispatching (PSD) is introduced, allowing for the flexible allocation of individual loads to distinct phases. Together, these coordinated technical solutions constitute a systematic optimization strategy. An algorithm is developed to harmonize the VSC-driven modeling for SOPs and BESSs with PSD, thereby improving the computational efficiency in managing power flow and phase balance. The results show that the proposed model significantly reduces losses and enhances the phase balance.**

***Index Terms*—Active distribution network, optimal power flow, soft open point, battery energy storage system, voltage source converter, Benders decomposition, phase-specific dispatching.**

Manuscript received: October 8, 2024; revised: February 3, 2025; accepted: April 14, 2025. Date of CrossCheck: April 14, 2025. Date of online publication: May 5, 2025.

This work was supported by Science and Technology Project of State Grid Corporation of China (No. 5400-202455203A-1-1-ZN).

C. Lou, R. Zhao, H. Zhang, L. Zhang, and W. Tang (corresponding author) are with the College of Information and Electrical Engineering, China Agricultural University, Beijing 100083, China (e-mail: chengwei.lou@cau.edu.cn; sy20233081956@cau.edu.cn; 18339797961@163.com; zhanglul@cau.edu.cn; wei_tang@cau.edu.cn).

J. Yang is with the James Watt School of Engineering, University of Glasgow, Glasgow, G12 8QQ, UK (e-mail: Jin.Yang@glasgow.ac.uk).

L. Zhang is with the State Grid Henan Economic Research Institute, Zhengzhou 450000, China (e-mail: zlinj@163.com).

DOI: 10.35833/MPCE.2024.001114

NOMENCLATURE

A. Parameters

ϵ	Pre-defined tolerance
σ	A positive number
γ^{VSC}	Loss coefficient for soft open point (SOP) of voltage source converter (VSC)
B_{eq}	Susceptance of VSC in an aggregated norm
C	Mechanical switching cost
E_m^{φ}	Open circuit voltage of battery energy storage system (BESS) of phase φ at tap m
G_{sw}	A conductance with a degree of power behavior
M	Number of tap positions
P_{PV}	Active power of photovoltaic (PV)
P_{load}	Active power of load
R_{int}	Internal resistance of a BESS
R_{sw}	Reciprocal of G_{sw}
$r_{\min}$, $r_{\max}$	The minimum and maximum ratios
r_t^{φ}	Tap ratio of a voltage regulator of phase φ at time t
Δr_i^{φ}	Ratio change per tap of phase φ on bus i
$S_{VSC,i}$	Capacity of VSC on bus i
$S_{rated,i}$	Rated capacity of BESS on bus i
$SOC_{\max}$	The maximum state of charge
$SOC_{\min}$	The minimum state of charge
$\bar{\boldsymbol{v}}_{i,t}$	Upper limit of voltage on bus i at time t
$\underline{\boldsymbol{v}}_{i,t}$	Lower limit of voltage on bus i at time t
$\boldsymbol{V}_0^{ref}$	Voltage vector on source bus
$\boldsymbol{v}_0^{ref}$	Second-order decision variable on source bus
V_{base}	Base voltage of distribution network
W_{δ}	Weight coefficient for phase-specific dispatching (PSD)
W_{α}, W_{β}, W_{γ}	Weight coefficients for each factor
$\boldsymbol{y}_j$	Shunt capacitance of bus j
$\boldsymbol{z}_{ij}$	Branch resistance from bus i to bus j

B. Variables

η	Continuous variable of lower bound objective
$\lambda^{\varphi,k}$	Lagrangian multiplier of phase φ at iteration k

θ_{lb}, θ_{ub} Lower and upper bounds of objective
$\mu^{\varphi}_{PY_i,i,n,t}$ Binary variable indicating PSD status of user n of phase φ on bus i at time t
ξ Slack variable of subproblem
$b^{\varphi}_{i,m}$ Binary variable of phase φ at tap m on bus i used to represent tap positions
C_{inv} Investment cost of SOP
C_{ope} Annual operational cost of SOP
C_{loss} Annual energy loss cost of SOP
e Continuous variable of sub-problem (SP)
$\boldsymbol{I}_{ij}$ Current vector from bus i to bus j
I^{φ}_{bat}, I_{sop} Currents of BESS of phase φ and SOP
$\boldsymbol{I}_{ij,t}$ Current from bus i to bus j at time t
m'_a Modulation index of VSC amplitude
$\bar{P}_{D,i,n,t}$ Active power demand of user n on bus i at time t
$P^{\varphi}_{D,i,t}$ Active power injection of phase φ on bus i at time t
$P^{\varphi}_{BESS,i,t}$ BESS charging power or discharging power of phase φ on bus i at time t
$P^{charge,\varphi}_{BESS,i,t}$ BESS charging power limit of phase φ on bus i at time t
$P^{discharge,\varphi}_{BESS,i,t}$ BESS discharging power limit of phase φ on bus i at time t
$P^{\varphi}_{VSC,i,t}$ Active power of VSC of phase φ on bus i at time t
$P^{\varphi}_{VSC,loss,i,t}$ Active power loss of VSC of phase φ on bus i at time t
$Q^{\varphi}_{D,i,t}$ Reactive power injection of phase φ on bus i at time t
$\bar{Q}_{D,i,n,t}$ Reactive power demand of user n on bus i at time t
Q^{φ}_{BESS} Reactive power of BESS of phase φ
$Q^{\varphi}_{VSC,i,t}$ Reactive power of VSC of phase φ on bus i at time t
r^{φ}_i Tap ratio of a transformer of phase φ on bus i
$\underline{R}_i$, $\bar{R}_i$ Lower and upper bounds of ratio on bus i
R_m Discrete tap ratio at tap m
$\boldsymbol{s}_j$ Power injection on bus j
$S_{BESS,i,t}$ Present state of energy storage on bus i at time t
$\boldsymbol{S}_{ij,t}$ Power from bus i to bus j at time t
$T_{i,m}$ Variable used for linear representation of bus i at tap m
V_{cap} Voltage of a capacitor in SOP
$\boldsymbol{V}_{i,t}$ Voltage vector on bus i at time t
$\boldsymbol{v}_{j,t}$ Voltage on bus j at time t
V^{φ}_{bat} Output voltage of battery of phase φ
$\boldsymbol{W}$ Column vector with R^2_m as elements
w Mixed-integer variable of master problem (MP)
x_i Square of amplitude modulation index of VSC on bus i
$\underline{x}_i$, $\bar{x}_i$ Lower and upper bounds of x_i

C. Indices and Sets

ϕ Set of all buses with PSD
ϕ_{PY_i}, ϕ_{PN_i} Sets of single-phase users with and without PSDs
Ω_b Set of all network branches
$\mathcal{E}$ Set of continuous variables
$\mathcal{N}$ Set of all buses
$\mathcal{N}^+$ Set of buses without substation
$\mathcal{N}_{SOP}$ Set of all buses with SOPs
$\mathcal{W}$ Set of binary variables
$\boldsymbol{A}$ Transformation matrix for symmetrical component method
abc Phase component
H Hermitian transpose

I. Introduction

DISTRIBUTION networks (DNs) cover vast geographical areas, resulting in an inherent three-phase imbalance [1]. The current evolution in energy consumption trends has led to a significant increase in single-phase domestic electric vehicle (EV) charging stations [2] and single-phase photovoltaic (PV) power systems within these DNs [3]. The unbalanced distribution of these loads across feeders leads to three-phase voltage and current imbalances in DNs. These imbalances can degrade power quality, increase power losses, and potentially damage the electrical appliances. Voltage imbalances, in particular, have a significant effect on the performance of induction motors, causing excessively high winding temperatures that accelerate the degradation of insulation material and significantly shorten the lifespan of the machine [4]. In addition, current imbalances contribute to higher distribution line losses and generate additional harmonic currents, further compromising power quality [5]. To address the imbalance in active DNs (ADNs) exacerbated by these developments, four existing domains have been identified: phase configuration adjustment, phase switch devices (PSDs), power electronic device utilization, and soft open point (SOP) applications.

In the domain of phase configuration adjustment, static approaches are emphasized. Both [6] and [7] examine data-driven phase identification in low-voltage systems, employing various clustering techniques. In addition, [8] investigates the optimal re-phasing of single-phase customers using a discrete genetic algorithm, analyzing its effects on power losses and voltage profiles. By contrast, [9] proposes a joint optimization model that incorporates Y-connected and other static reactive power compensation devices for network balancing. Nevertheless, further research is required to develop more adaptable optimization strategies that can effectively respond to the evolving demands of ADNs.

PSDs provide a dynamic approach to load balancing by assigning single-phase consumers to specific phases. Studies have shown that under limited data and communication conditions, the relationship between voltage imbalance sensitivity and power injection supports the local control strategies for PSDs on discrete buses [10]-[12]. To address the imbalance issues exacerbated by PV generation, [13] introduces an iteration-based algorithm to optimize phase connections, addressing the mixed-integer non-convex programming problem. Another study in [14] highlights the cost and efficiency benefits of automatic re-phasing compared with manual approaches in smart DNs, and proposes an optimal balancing technique using the modified shuffled frog-leaping algorithm. However, despite previous validation, the algorithms have been tested on modest validation systems, which may

not be sufficient for achieving optimal solutions as system dimensions and complexity grow. The introduction of integer variables further complicates the resolution process, underscoring the need for a more efficient algorithm.

Power electronic devices in DNs enable dynamic balancing. Static var compensators (SVCs) redistribute currents among phases [15], whereas step voltage regulators control the voltage magnitudes to mitigate voltage imbalances and minimize power losses [16], [17]. Distributed generators (DGs) adjust the power injection to maintain voltage balance, and [18] explores the three-phase adjustment capabilities of DG inverters. References [19] and [20] focus on PV systems for local voltage balancing and coordinated multiple microgrid strategies. Finally, [21] and [22] investigate the per-phase control of three-phase DG inverters and DG aggregation to enhance the performance and flexibility of DN. Despite their balancing capabilities, these devices are typically preset and lack the ability required for interphase power transfer.

SOPs can achieve advanced balancing in ADNs, distinguishing them from conventional devices such as SVCs and PV inverters [23]. SOPs connect different buses through a shared DC link, allowing for active power transfer that exceeds conventional power flow constraints [13], which in turn aids in DG integration and network balancing. References [24] and [25] have introduced a multi-objective operational model to evaluate the balancing efficacy of SOPs. References [24], [26], and [27] have emphasized the role of SOPs in mitigating voltage violations and uncertainties associated with PV outputs in ADNs. The phase-changing SOPs (PC-SOPs) [28], [29] and a coordination strategy that utilizes phase-switching SOPs (PS-SOPs) and PSDs [30] have been introduced to enhance the network balancing. Both PS-SOP and PC-SOP can perform phase switching; however, PS-SOPs enable the real-time cross-phase power transfer through PSDs, providing more flexibility. In addition, [31] pioneers a phase-transfer technique in MATLAB Simulink to re-distribute single-phase power across multiple phases, showcasing a novel approach to phase power management.

The aforementioned approaches are commonly used infrastructures in DNs. Despite limitations in manufacturing and control algorithms, phase-switching (PS) devices provide an effective solution and remain a significant focus due to their practical performance. By contrast, the capacitor-based devices are limited to discrete adjustments and lack real-time responsiveness, whereas power electronic devices allow for continuous regulation and rapid response, offering superior performance in mitigating three-phase imbalance.

In summary, as an emerging power electronic component, SOPs significantly mitigate imbalances in ADNs, and their interactions with other components such as PSDs are examined in this paper. The research gap in existing SOP models lies in their tendency to simplify the intertwined constraints between active and reactive power [32], resulting in an unrealistic assumption that they can be generated independently. By contrast, the active-reactive power dispatch model recognizes the AC power flow constraints inherent in SOPs. As described in [32], the voltage source converter (VSC)-driven battery energy storage system (BESS) provides insight into the interplay between the output voltage of pulse width modulation (PWM) control of VSCs and the output power of BESS. This understanding has expanded with the advent of VSC-driven energy routers [33]. However, although AC models of SOPs consider reactive power, they fail to exploit the potential of DC components. This limitation particularly affects the synchronization of renewable generation across different DC buses with individual VSC operations, hindering the effective integration of renewable energy into three-phase systems. The introduction of PSDs adds complexity due to the presence of integer variables. Their discrete nature complicates switching operations, thus requiring advanced algorithmic solutions. This paper describes the challenges faced by ADNs from emerging single-phase loads, reviews the current mitigation strategies, identifies the research gaps, and presents advanced control techniques.

The primary contributions of this paper are as follows.

1) Component incorporation: this paper enhances the foundational SOP model by integrating PWM technology with the VSC component, resulting in VSC-driven modeling for the SOPs and BESSs to balance three-phase DNs. This integration improves the model accuracy by clarifying the interaction between the output voltage of PWM control of VSCs and the output power of BESSs, capturing the explicit circuit relationship for more precise regulation. In addition, it accounts for utility voltage changes to further refine the power regulation. By positioning these components on buses with significant power imbalances, this paper demonstrates improved efficiency and highlights the advantages of the proposed model.

2) Performance improvement: this paper proposes a novel VSC-driven model of both SOPs and BESSs that work seamlessly with PSDs. This collaboration effectively reduces power losses across the DN and significantly improves the three-phase balance of the system. The proposed model demonstrates increased efficiency and strong potential for implementation in real-world DN applications.

3) Optimization strategy: this paper presents a systematic optimization strategy for balancing three-phase power systems, integrating PSDs, BESS, and SOPs. It starts by addressing the key system parameters and placement of BESS and SOPs, then progresses to the construction of three-phase VSC-driven models. The optimization strategy utilizes symmetrical semi-definite programming (SDP), incorporating convex relaxation to develop a mixed-integer SDP (MISDP). In addition, this paper introduces an efficient algorithm based on Benders decomposition (BD) enhanced with a bound-tightening strategy to solve the problem effectively.

The remainder of this paper is structured as follows. Section II details the methodology of this paper, beginning with an explanation of the theoretical foundations including the principles of VSC and PWM technologies, and then describing the control relationship between these technologies and the model parameters. Section III presents case studies exploring various scenarios, facilitating the comparison and result analysis for evaluating the effectiveness of the proposed model. Section IV concludes this paper.

II. Methodology

Figure 1 illustrates the architecture of the analyzed DN. Three components are used to optimize the power dispatching, i.e., BESS used for energy storage and dispatching, PSD employed for effective load management, and PV highlighting the effects of DG. Additional model preliminaries can be found in Supplementary Material A.

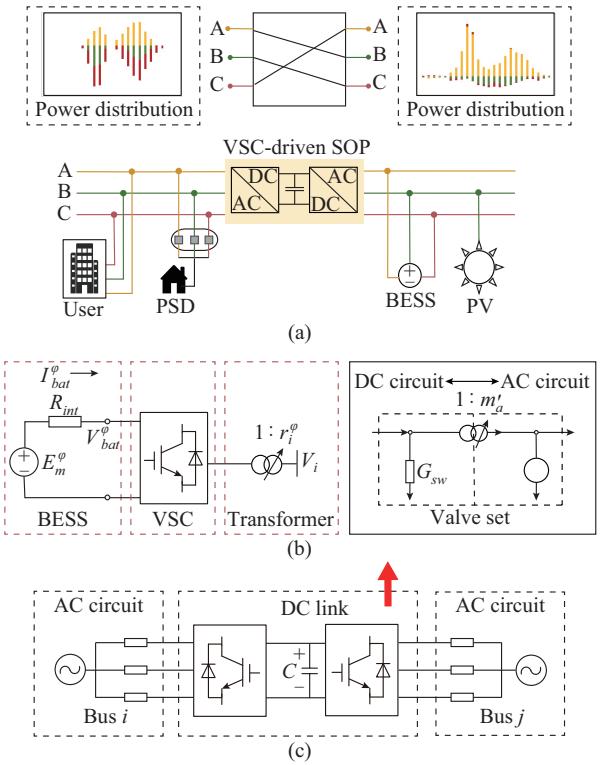

Fig. 1. Architecture of analyzed DN. (a) Overall architecture. (b) Equivalent circuit of BESS. (c) Equivalent circuit of three-phase VSC-driven SOP.

A. Optimal Power Flow of Three-phase AC DNs

For each line segment from bus i to bus j, the vectors of bus voltages are defined as $\boldsymbol{V}_i$ and $\boldsymbol{V}_j$, and the vector of current is defined as $\boldsymbol{I}_{ij}$. The second-order decision variables are defined as $\boldsymbol{v}_i=\boldsymbol{V}_i\boldsymbol{V}_i^H$, $\boldsymbol{l}_{ij}=\boldsymbol{I}_{ij}\boldsymbol{I}_{ij}^H$, and $\boldsymbol{S}_{ij}=\boldsymbol{V}_i\boldsymbol{I}_{ij}^H$.

The symmetrical SDP model is employed due to its superior numerical precision compared with the traditional model [34]. We then index the substation bus by 0 and the other buses by 1, 2, …, n. Let $\mathcal{N}$ denote the set of all buses and $\mathcal{N}^+=\mathcal{N}\backslash\{0\}$. The voltages in the phase components are transformed into symmetrical components as [35]:

$$\boldsymbol{V}_{i,t}^{abc}=\boldsymbol{A}\boldsymbol{V}_{i,t}^{012} \tag{1}$$

$$\boldsymbol{A}=\frac{1}{\sqrt{3}}\begin{bmatrix}1 & 1 & 1\\ 1 & a^2 & a\\ 1 & a & a^2\end{bmatrix} \tag{2}$$

where $a=1\angle 120°$; and superscript 012 refers to the zero-, positive-, and negative-sequence components in symmetrical component theory, respectively. Consequently, the three-phase variables and impedance parameters are correlated with the equivalent variables in the symmetrical components as:

$$\begin{cases}\boldsymbol{v}_{i,t}^{abc}=\boldsymbol{V}_{i,t}^{abc}\boldsymbol{V}_{i,t}^{abc,H}=\boldsymbol{A}\boldsymbol{V}_{i,t}^{012}(\boldsymbol{A}\boldsymbol{V}_{i,t}^{012})^H=\boldsymbol{A}\boldsymbol{v}_{i,t}^{012}\boldsymbol{A}^H\\ \boldsymbol{l}_{ij,t}^{abc}=\boldsymbol{A}\boldsymbol{l}_{ij,t}^{012}\boldsymbol{A}^H\\ \boldsymbol{S}_{ij,t}^{abc}=\boldsymbol{A}\boldsymbol{S}_{ij,t}^{012}\boldsymbol{A}^H\\ \boldsymbol{z}_{ij,t}^{abc}=\boldsymbol{A}\boldsymbol{z}_{ij,t}^{012}\boldsymbol{A}^{-1}=\boldsymbol{A}\boldsymbol{z}_{ij,t}^{012}\boldsymbol{A}^H\\ \boldsymbol{y}_{i,t}^{abc}=\boldsymbol{A}\boldsymbol{y}_{i,t}^{012}\boldsymbol{A}^{-1}=\boldsymbol{A}\boldsymbol{y}_{i,t}^{012}\boldsymbol{A}^H\end{cases} \tag{3}$$

where $\boldsymbol{A}^H=\boldsymbol{A}^{-1}$. The structure of the branch impedance matrix in the sequence system is related to the self-impedance and mutual impedance of the branches in the phase system. As stated in [36], in most computations, to decouple the sequences, it is assumed that the self-impedances and mutual impedances are equal within each phase and between phases, respectively, thus obtaining a diagonalized matrix.

Consequently, the power flow balance constraint at time t is given as:

$$\sum_{ij\in\Omega_b} diag(\boldsymbol{A}(\boldsymbol{S}_{ij,t}^{012}-\boldsymbol{z}_{ij}^{012}\boldsymbol{l}_{ij,t}^{012})\boldsymbol{A}^H)+\boldsymbol{s}_{j,t}+\boldsymbol{y}_{j,t}^{012}\boldsymbol{v}_{j,t}^{012}=\sum_{jk\in\Omega_b} diag(\boldsymbol{A}\boldsymbol{S}_{jk,t}^{012}\boldsymbol{A}^H) \tag{4}$$

The Kirchoff's voltage law along line ij at time t is expressed as:

$$\boldsymbol{v}_{j,t}^{012}=\boldsymbol{v}_{i,t}^{012}-(\boldsymbol{S}_{ij,t}^{012}\boldsymbol{z}_{ij}^{012,H}+\boldsymbol{S}_{ij,t}^{012,H}\boldsymbol{z}_{ij}^{012})+\boldsymbol{z}_{ij}^{012}\boldsymbol{l}_{ij,t}^{012}\boldsymbol{z}_{ij}^{012,H} \tag{5}$$

Equation (6) imposes lower and upper limits on the voltage of bus i at time t, whereas (7) defines the voltage on the source bus. Equation (8) expresses the positive semi-definite constraint by:

$$\underline{\boldsymbol{v}}_{i,t}\le diag(\boldsymbol{A}\boldsymbol{v}_{i,t}^{012}\boldsymbol{A}^H)\le\bar{\boldsymbol{v}}_{i,t}\quad i\in\mathcal{N} \tag{6}$$

$$\boldsymbol{v}_0^{012}=\boldsymbol{V}_0^{012,ref}(\boldsymbol{V}_0^{012,ref})^H \tag{7}$$

$$\begin{bmatrix}\boldsymbol{v}_i^{012} & \boldsymbol{S}_{ij}^{012}\\ \boldsymbol{S}_{ij}^{012,H} & \boldsymbol{l}_{ij}^{012}\end{bmatrix}\succcurlyeq\boldsymbol{0}\quad i\to j \tag{8}$$

Single- and two-phase branches are modeled as equivalent three-phase lines, using dummy lines and buses to maintain the three-phase structure [37]. This allows their representation in sequence networks. The series impedances of these dummy lines can be assigned arbitrary values. Consequently, the conversion of symmetrical component variables back to phase variables is applied for buses connected to single- or two-phase branches [34].

Finally, the symmetrical SDP model is subject to constraints (9)-(13) for single- and two-phase branches, and constraints (4)-(8) for three-phase backbones.

$$\sum_{ij\in\Omega_b} diag(\boldsymbol{S}_{ij,t}-\boldsymbol{z}_{ij}\boldsymbol{l}_{ij,t})+\boldsymbol{s}_{j,t}+\boldsymbol{y}_{j,t}\boldsymbol{v}_{j,t}=\sum_{jk\in\Omega_b} diag(\boldsymbol{S}_{jk,t}) \tag{9}$$

$$\boldsymbol{v}_{j,t}=\boldsymbol{v}_{i,t}-(\boldsymbol{S}_{ij,t}\boldsymbol{z}_{ij}^H+\boldsymbol{S}_{ij,t}^H\boldsymbol{z}_{ij})+\boldsymbol{z}_{ij}\boldsymbol{l}_{ij,t}\boldsymbol{z}_{ij}^H \tag{10}$$

$$\underline{\boldsymbol{v}}_{i,t}\le diag(\boldsymbol{v}_{i,t})\le\bar{\boldsymbol{v}}_{i,t}\quad i\in\mathcal{N} \tag{11}$$

$$\boldsymbol{v}_0=\boldsymbol{V}_0^{ref}(\boldsymbol{V}_0^{ref})^H \tag{12}$$

$$\begin{bmatrix}\boldsymbol{v}_{i,t} & \boldsymbol{S}_{ij,t}\\ \boldsymbol{S}_{ij,t}^H & \boldsymbol{l}_{ij,t}\end{bmatrix}\succcurlyeq\boldsymbol{0}\quad i\to j \tag{13}$$

B. Modeling of Three-phase VSC-driven SOP

In the model shown in Fig. 1(a), we present a three-phase VSC-driven SOP that includes an AC/DC VSC, DC capaci-

tor, and DC/AC VSC. As depicted in Fig. 1(c), the operation of the VSC can be compared with that of an ideal complex tap-changing transformer [33].

The foundational relationship inherent to the PWM controlled operation of VSCs is expressed as:

$$\begin{cases} \left|V_i^{\varphi}\right| \le m_a' \left|V_{cap}\right| \\ \left|V_j^{\varphi}\right| \le m_a' \left|V_{cap}\right| \end{cases} \tag{14}$$

The VSC adheres to the relationship m_a' outlined in [32]. The switching losses of the converter can be quantified as [32]:

$$P_{VSC,loss}^{\varphi} = G_{sw} V_{cap}^2 \tag{15}$$

The VSC is modeled as a combination of a resistor and a reactive power source, as shown in Fig. 1(c). The resistor connects to the resistive component of power grid, while the reactive power source provides only reactive power to the AC converter buses, enhancing the reactive power compensation capability.

The operation of the three-phase VSC-driven SOP is limited by capacity constraints and power losses, which can be expressed by:

$$\left\| P_{VSC,i,t}^{\varphi}, Q_{VSC,i,t}^{\varphi} \right\|_2 \le S_{VSC,i} \tag{16}$$

$$\sum_{\varphi} (P_{VSC,i,t}^{\varphi} + P_{VSC,loss,i,t}^{\varphi}) + \sum_{\varphi} (P_{VSC,j,t}^{\varphi} + P_{VSC,loss,j,t}^{\varphi}) = 0 \tag{17}$$

C. Modeling of Three-phase VSC-driven BESS

A three-phase VSC-driven BESS model is adopted. However, the power can be managed separately by phase. As shown in Fig. 1(b), the simplified circuits of the individual phases of the VSC-driven BESS model include three essential elements: VSC, battery, and transformer [38]. The internal circuit of the battery adheres to the equation that $V_{bat}^{\varphi} = E_m^{\varphi} - I_{bat}^{\varphi} R_{int}$, and V_{bat}^{φ} is approximated to E_m^{φ} [32], which means that internal losses are not factored into the constraints but are optimized in the objective function. Consequently, the power flow and output voltage satisfy the following equations.

$$\begin{cases} P_{BESS}^{\varphi} = E_m^{\varphi} I_{bat}^{\varphi} \\ Q_{BESS}^{\varphi} = (m_a')^2 B_{eq} (E_m^{\varphi})^2 \\ \left|V_i^{\varphi}\right| = m_a' r_i^{\varphi} E_m^{\varphi} \end{cases} \tag{18}$$

Specifically, r_i^{φ} is modeled as shown in (19) with binary variables [39].

$$r_i^{\varphi} = \sum_{m=0}^{M} R_m b_{i,m}^{\varphi} = \sum_{m=0}^{M} (r_{min} + \Delta r_i^{\varphi} m) b_{i,m}^{\varphi} \tag{19}$$

The sum of $b_{i,m}^{\varphi}$ to 1 yields a single ratio:

$$\sum_{m=0}^{M} b_{i,m}^{\varphi} = 1 \quad b_{i,m}^{\varphi} \in \{0,1\} \tag{20}$$

As $\sum_{m=0}^{M} b_{i,m}^{\varphi} = 1$, only a single $b_{i,m}^{\varphi}$ is equal to 1, with the rest being 0. And since $(b_{i,m}^{\varphi})^2 = b_{i,m}^{\varphi}$, we have $(r_i^{\varphi})^2 = \sum_{m=0}^{M} R_m^2 b_{i,m}^{\varphi} = \boldsymbol{W}^{\mathrm{T}} b_i^{\varphi}$.

Equation (18) is nonconvex because it is the product of a continuous variable and a discrete variable for $\left|V_i^{\varphi}\right|$. Following the variable alteration, it can be reformulated as:

$$v_i^{\varphi} = V_i^{\varphi 2} = (m_a')^2 (r_i^{\varphi})^2 (E_m^{\varphi})^2 = x_i (r_i^{\varphi})^2 (E_m^{\varphi})^2 = \boldsymbol{W}^{\mathrm{T}} (E_m^{\varphi})^2 x_i b_i^{\varphi} \tag{21}$$

The nonlinear product $x_i b_i^{\varphi}$ is represented by $T_{i,m}$ as:

$$T_{i,m} = x_i b_i^{\varphi} \quad i \in \mathcal{N}_B \tag{22}$$

Based on [32], (22) can be replaced by the following constraints:

$$\underline{x}_i b_i^{\varphi} \le T_{i,m} \le \bar{x}_i b_i^{\varphi} \tag{23}$$

$$\underline{x}_i (1 - b_i^{\varphi}) \le x_i - T_{i,m} \le \bar{x}_i (1 - b_i^{\varphi}) \tag{24}$$

The BESS operational constraints are expressed as:

$$\begin{cases} S_{BESS,i,t} = S_{BESS,i,t-1} + \sum_{\varphi} P_{BESS,i,t}^{\varphi} \\ \left| P_{BESS,i,t}^{charge,\varphi} \right| \le \left| P_{BESS,i,t}^{\varphi} \right| \le \left| P_{BESS,i,t}^{discharge,\varphi} \right| \\ SOC_{\min} \le S_{BESS,i,t} S_{rated,i}^{-1} \le SOC_{\max} \end{cases} \tag{25}$$

The power loss of the three-phase VSC-driven BESS follows (15).

D. Integration of PSD

For a specific bus designated as i, consumers (represented by ϕ) can be divided into two categories: those equipped with a PSD, represented by ϕ_{PY_i}, and those not in possession of these devices, represented by ϕ_{PN_i}. The latter subset is further stratified based on their connected phases into $\phi_{PN_i^a}$, $\phi_{PN_i^b}$, and $\phi_{PN_i^c}$. Consequently, the power injection for a bus equipped with a PSD can be expressed as [30]:

$$\begin{cases} P_{D,i,t}^{\varphi} + \mathrm{j} Q_{D,i,t}^{\varphi} = \sum_{n \in \phi_{PN_i}^{\varphi}} (\bar{P}_{D,i,n,t} + \mathrm{j} \bar{Q}_{D,i,n,t}) + \\ \qquad \sum_{n \in \phi_{PY_i}} \mu_{PY_i,i,n,t}^{\varphi} (\bar{P}_{D,i,n,t} + \mathrm{j} \bar{Q}_{D,i,n,t}) \\ \sum_{\varphi} \mu_{PY_i,i,n,t}^{\varphi} = 1 \quad i \in \phi, n \in \phi_{PY_i}, \forall t \\ \mu_{PY_i,i,n,t}^{\varphi} \in \{0,1\} \quad i \in \phi, n \in \phi_{PY_i}, \forall t \end{cases} \tag{26}$$

E. Overall Optimization Problem Using BD

Continuous and binary variables are denoted as $e = \{v, S, \ell\} \in \mathcal{E}$ and $w = \{r, T, b, \mu\} \in \mathcal{W}$, respectively.

The network loss function is expressed as:

$$F(e) = W_\alpha F_1 + W_\beta F_2 + W_\gamma F_3 \tag{27}$$

The calculation formulas for the losses of the line, SOP, and BESS are represented by F_1, F_2, and F_3 in (28)-(30), respectively:

$$F_1 = \sum (P_D + P_{BESS} + P_{PV} - P_{load}) \tag{28}$$

$$F_2 = I_{sop}^2 (R_{sw} + R_{int}) \tag{29}$$

$$F_3 = I_{bat}^2 (R_{sw} + R_{int}) \tag{30}$$

Directly solving MISDP is particularly complex due to the inclusion of integer decision variables, which often leads to computational infeasibility. This challenge can be effectively addressed through BD [40], where the original problem is di-

vided into a mixed-integer linear programming master problem (MP) and an SDP subproblem (SP), which can be solved iteratively. This approach mitigates issues of local optimality associated with integer decision variables and ensures the convergence of the algorithm [41]. In addition, the iterative process, which gradually approaches the optimal solution, significantly improves computational efficiency [42]. Consequently, BD is employed in this study to decouple and solve the original problem effectively. In each iteration, the solution to the binary variable from the MP is passed to the SP, and that from the SP generates an optimality cut for the MP.

Furthermore, a bound-tightening (BT) strategy is employed to solve the ratio bounds faster [39]. This outcome serves as a constraint on the MP, ensuring that the MP solution is always feasible for the SP, thereby eliminating the generation of feasible cuts.

$$\begin{cases} \text{BT: min (or max)} \displaystyle\sum_{i\in\mathcal{N}^+}\sum_{\varphi} v_i^{\varphi} \\ \text{s.t. } \underline{x}_i (E_m^{\varphi})^2 \le v_i^{\varphi} \le \bar{x}_i (E_m^{\varphi})^2 \quad \forall \varphi, i \in \mathcal{N}^+ \\ \quad (4)\text{-}(8) \end{cases} \tag{31}$$

The ratio bounds are computed as $\underline{R}_i(\overline{R}_i) = v_i^{\varphi}/(x_i (E_m^{\varphi})^2)^2$.

Given the cost associated with mechanical switching [40], MP is formulated as:

$$\begin{cases} \text{MP: } \theta_{lb} = \min(\eta + Cw) \\ \text{s.t. } \eta \ge F(e^*) + \displaystyle\sum_{i\in\mathcal{N}^+}\sum_{\varphi} \lambda^{\varphi,k} \boldsymbol{W}^{\mathrm{T}\prime} (w_i^{\varphi} - w_i^{\varphi,k}) \quad k \in \mathcal{N}^+ \\ \quad \underline{R}_i \le \boldsymbol{W}^{\mathrm{T}} b_i^{\varphi} \le \bar{R}_i \quad \forall \varphi, i \in \mathcal{N}^+ \\ \quad (19), (20), (23), (24), (26) \quad w \in \mathcal{W} \end{cases} \tag{32}$$

The superscript * distinguishes the quantities obtained from the SP, and $\boldsymbol{W}^{\mathrm{T}\prime} = \begin{bmatrix} \boldsymbol{W}^{\mathrm{T}} \\ W_{\delta} \end{bmatrix}$. In comparison to line losses, the costs associated with the modulation of the VSC and PSD are minimal and can be overlooked. The optimal objective of MP establishes a lower bound θ_{lb}. Here, W_{δ} is the weight coefficient for PSD. The solution of MP $\hat{w}$ is guaranteed to be feasible for SP when the BT is solved. For the SP, the slack variable ξ is added to the return optimality cuts, where $\sigma \gg 0$ [43]:

$$\begin{cases} \text{SP: } \theta_{ub} = \min(F(e) + \sigma\xi) \\ \text{s.t. } \xi \ge 0 \\ \quad (4)\text{-}(13), (21), (23), (25) \quad e \in \mathcal{E}, \hat{w} \in \mathcal{W} \end{cases} \tag{33}$$

If the SP has a solution to b_i^{φ} obtained from the MP, the optimal objective for SP is an upper bound θ_{ub} for the original problem. In addition, it generates optimal Lagrangian multipliers $\lambda^{\varphi,k}$ associated with the binary variables to create optimality cuts that constrain the MP, where k denotes the iteration. The optimality of the solution is measured by the gap between θ_{lb} and θ_{ub}. The problems iterate until the predefined tolerance ϵ for the gap is satisfied, thereby achieving the optimal solution [44].

The entire operation optimization process for the MISDP problem is illustrated in Algorithm 1, which outlines a systematic approach for optimizing a three-phase DN. First, the basic parameters of the network are input, and component modeling is conducted. Through the use of the symmetrical SDP method, convex relaxation techniques are applied, followed by three-phase decoupling. Benders decomposition is then employed to solve the MISDP problem. The algorithm checks the necessity of PSD optimization, and if necessary, reformulates the MP. The resulting optimal solution is also subjected to a convergence check. Finally, the process either concludes or returns to the optimization step.

Algorithm 1: operation optimization process for MISDP problem

```
Initialization:
    Input initial three-phase parameters
    Specify the locations of BESS and SOP
Model setup:
    Construct three-phase VSC-driven SOP/BESS model
    Define the objective function and constraints
    Use the symmetrical SDP method to perform three-phase decoupling
BD:
    Pick any b_i^φ ∈ W and initialize θ_lb^0 = −∞ and θ_ub^0 = ∞
    Solve BT to obtain R_i and R̄_i
while ε ≤ |θ_ub^k − θ_lb^k| do
    Solve MP(R_i, R̄_i) and update θ_lb^k and ŵ
    Solve SP, update θ_ub^k, and generate optimality cuts
end while
Initialize the phase setting of PSD
if PSD optimization is not required then
    Terminate algorithm
end if
PSD optimization:
    Formulate the new MP by updating W_δ from an initial value of 0 and
      add constraint (26)
    Obtain the action decisions
if |θ_ub^k − θ_lb^k| < ε then
    Terminate algorithm
else
    Update outputs of SOP, BESS, and PSD
    Return to re-optimization
end if
```

F. Practical Challenges of SOP

Although the use of SOPs enhances ADN operation and decreases power losses, the associated costs of deploying these devices require further investigation [45]. To assess the economic feasibility of the proposed model, the savings from reduced power loss costs are compared with the implementation costs, which encompass both investment and operational expenses. The proposed model is considered feasible if the savings are equal to or greater than the costs [46]. The cost formulas and relevant parameters are derived from [47] and are detailed in Supplementary Material B.

III. Case Study

Based on a previous study [29], a three-phase VSC-driven SOP is conducted using an adapted IEEE 123-bus DN, as illustrated in Fig. 2(a). The network incorporates 10 strategically positioned PV systems across various buses. Specifically, SOP1 and SOP2 are connected between buses 151 and 300 with a capacity of 150 kVA and between buses 54 and 93 with a capacity of 300 kVA, respectively. The BESS has a cumulative capacity of 1.50 MVA. $B_{eq} = 0.001$ S, $R_{sw} = 0.2$ p.u., $R_{int} = 0.44$ p.u., and $E_m = \sqrt{2}\, V_{base}$. The three-phase active power of the load is shown in Fig. 2(b), where the reac-

tive power trend aligns with it. The PV output profile is consistent with the patterns shown in Fig. 2(c). Voltage regulators are tuned as: for buses 150-149 (three-phase), $[r_t^a, r_t^b, r_t^c]$=[1.04375, 1.04375, 1.04375]; for buses 9-14 (single-phase), $r_t^a = 0.99375$; for buses 25-26 (two-phase), $[r_t^a, r_t^c]$=[1, 0.99375]; and for buses 67-160 (three-phase), $[r_t^a, r_t^b, r_t^c]$=[1.05, 1.00625, 1.03125]. The voltage constraints for all buses are set to be [0.94, 1.10]p. u.. The symmetric SDP approach is implemented using the YALMIP toolbox [48] and optimized using the MOSEK solver. A 34-bus validation case is presented in Supplementary Material C.

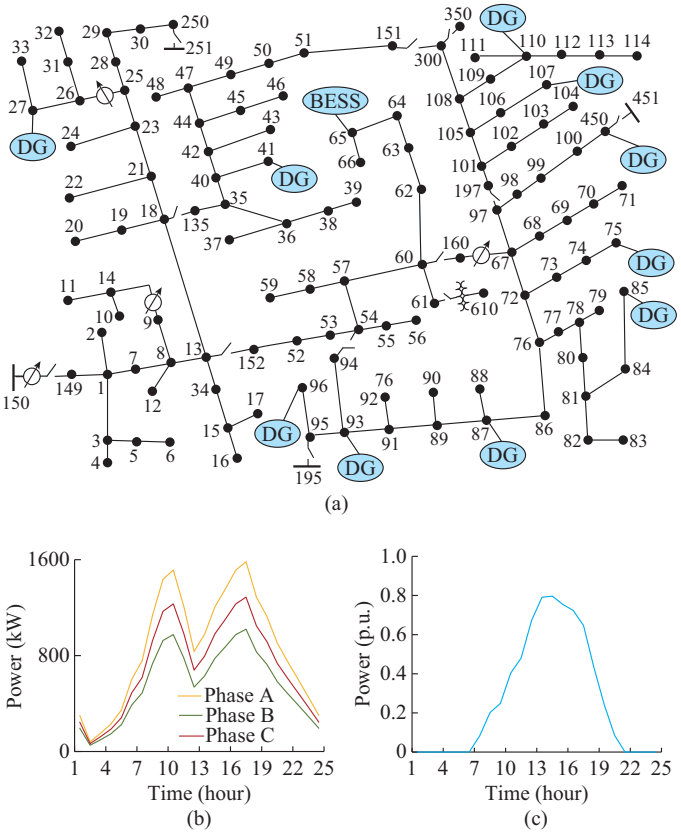

Fig. 2. Topology, load profile, and PV output profile. (a) Topology of IEEE 123-bus DN. (b) Three-phase active power of load. (c) PV output profile.

A. Comparative Analysis of Traditional and Three-phase VSC-driven SOP Models

For the traditional SOP, the fixed loss coefficient for an SOP is assumed to be $\gamma^{VSC} = 0.02$, as proposed in [49]. The loss of the SOP is represented by:

$$P^{\varphi}_{VSC,loss,i,t} = \gamma^{VSC} \sqrt{(P^{\varphi}_{VSC,loss,i,t})^2 + (Q^{\varphi}_{VSC,loss,i,t})^2} \tag{34}$$

To illustrate the advantages of the three-phase VSC-driven SOP, we present two representative cases (Cases A and B) detailed as follows. The comparison incorporates a BESS in both charging and discharging modes.

1) Case A: traditional SOP interfacing buses 151-300 (SOP1) and buses 54-93 (SOP2) [49].

2) Case B: three-phase VSC-driven SOP connecting buses 151-300 (SOP1) and buses 54-93 (SOP2).

Table I compares the performance metrics of the traditional SOP (Case A) with the three-phase VSC-driven SOP (Case B) for both SOP1 and SOP2, revealing several critical insights. Notably, losses and power output are calculated over a 24-hour period, with active power representing the total power transmitted across the phases. First, transitioning from Case A (0.7382 MW) to Case B (0.7302 MW) results in a clear reduction in line loss, indicating improved efficiency with the three-phase VSC-driven SOP. In addition, Case B significantly increases the transmission of active power, particularly for SOP2, which shows an increase of 978.49 kW compared with Case A. The loss percentage in Case B, defined as the ratio of SOP losses to active power, is more efficient (2.39%) for SOP2 compared with 4.35% in Case A. Furthermore, in Case B, SOP1 demonstrates a significant increase in reactive power supply, with values of 890.31 kvar, up from 352.26 kvar in Case A. Another important metric is the three-phase imbalance index, which can be calculated as detailed in [29]. In Case B, the three-phase VSC-driven SOP shows a reduction in this index to 7.07×10^{-2}, down from 8.58×10^{-2} in Case A, indicating better system balance. In summary, the data in Table I support the conclusion that the three-phase VSC-driven SOP (Case B) offers superior efficiency and operational benefits compared with the traditional SOP, particularly when assessing the cumulative performance of both SOP1 and SOP2.

TABLE I
COMPARATIVE ANALYSIS OF PERFORMANCE METRICS OF TRADITIONAL AND THREE-PHASE VSC-DRIVEN SOPS

Case	SOP	Line loss (MW)	Imbalance index (10^{-2})	SOP active power (kW)	SOP reactive power (kvar)	SOP loss (kW)
Case A	SOP1	0.7382	8.58	113.91	352.26	8.37
	SOP2	0.7382	8.58	396.89	234.97	17.28
Case B	SOP1	0.7302	7.07	302.72	890.31	12.21
	SOP2	0.7302	7.07	1375.38	484.24	32.84

Figures 3 and 4 illustrate the three-phase power generation of the traditional and proposed models, respectively. In terms of SOP1 in Case A, the initial morning hours from 01:00 to 07: 00 show a notably reserved pattern of active power transfer. The most significant peak occurs at 07: 00, where Phase A of bus 151 reaches 0.05537 kW. However, at 08:00, a marked increase in power transfer dynamics is evident. This upward trend culminates at 10:00, when Phase A of bus 300 records a significant active power transfer of 20.55 kW. This sharp rise is later followed by a period of relative inactivity from 11: 00 to 15: 00, during which the transfer values approach zero. The peak of power transfer for SOP1 is reached at 17:00: Phase C of bus 151 registers –26.40 kW, simultaneously transferring –26.40 kW to Phase A of bus 151 (recorded at 6.65 kW) and to Phase A of bus 300 (recorded at 18.28 kW). By examining the reactive power metrics, Phase A of bus 151 displays two significant peaks: 76.28 kvar at 10:00 and a heightened 92.07 kvar at 17:00. As the system transitions into the evening hours, specifically from 19:00 to 24:00, a decline in both active and reactive power transfers is observed, with values largely con-

fined to the range of 1×10^{-5} to 1×10^{-6}.

In the appraisal of SOP2 for Case A, the early hours from 01:00 to 07:00 show an active power transfer trend similar to SOP1. Notably, by 07:00, Phase A of bus 151 reaches a peak that aligns with this scenario. At 08:00, a significant increase in power transfer is observed. This pattern peaks by 10:00, when Phase A of bus 300 records an active power transfer of 56.06 kW.

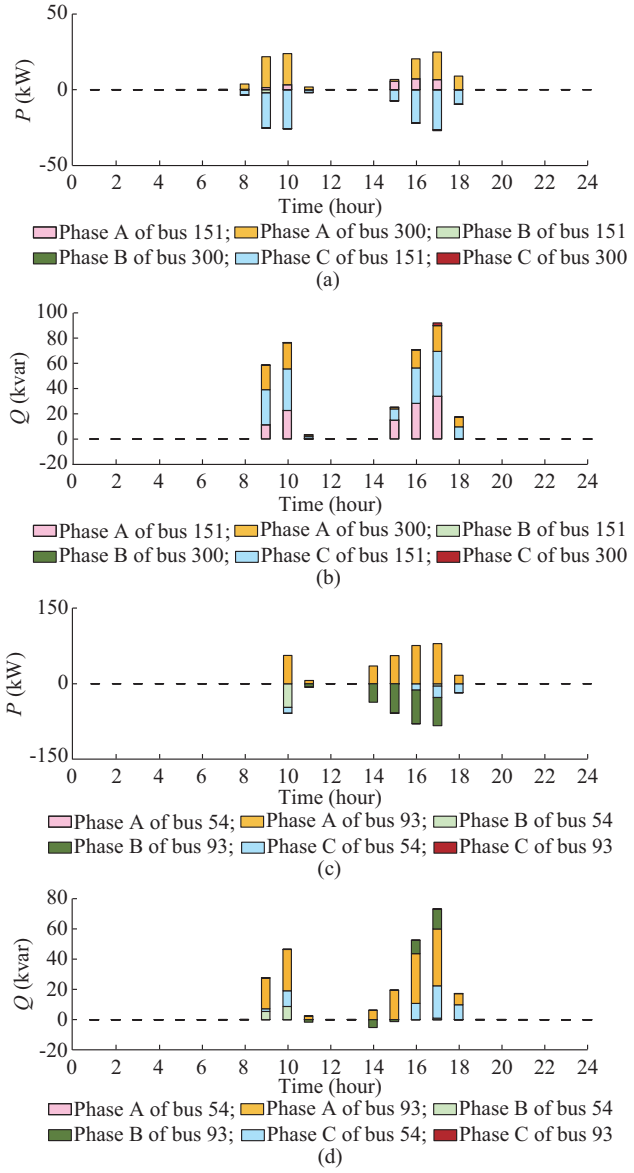

Fig. 3. Three-phase power generation of traditional model. (a) Active power of SOP1. (b) Reactive power of SOP1. (c) Active power of SOP2. (d) Reactive power of SOP2.

In the following interval, from 11:00 to 15:00, the trend mirrors that of SOP1, registering near-zero transfer values. The highest power transfer for SOP2 occurs at 17:00, with Phase A of bus 93 transferring a notable power of 79.64 kW. Subtle variations in the reactive power data for Phase A of bus 151 are noted, but it maintains a similar bifurcated peak structure to SOP1. As the evening hours progress from 19:00 to 24:00, a clear decrease in both active and reactive power transfers occurs, primarily converging within the range of 1×10^{-5} to 1×10^{-6}.

In terms of SOP1 within Case B, the active power transmission is minimal during the early morning hours (from 01:00 to 05:00), totaling 8.10 kW. However, between 06:00 and 10:00, a notable surge in power generation occurs in Phase A of bus 300, reaching peak values of 27.20 kW and 26.80 kW at 09:00 and 10:00, respectively.

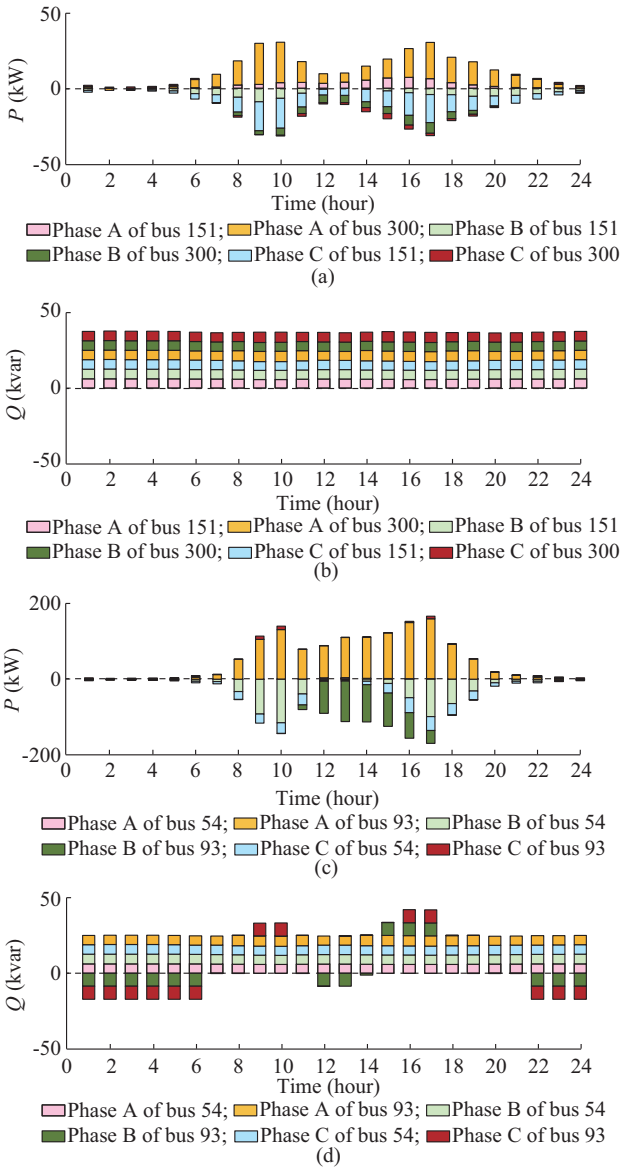

Fig. 4. Three-phase power generation of proposed model. (a) Active power of SOP1. (b) Reactive power of SOP1. (c) Active power of SOP2. (d) Reactive power of SOP2.

From 11:00 to 13:00, the power output in the phase C experiences a slight decline, stabilizing at 4.60 kW. Nevertheless, from 14:00 to 17:00, it rebounds, peaking at 18.60 kW by 17:00. Following this period (from 06:00 to 12:00), power gradually decreases to merely 1.20 kW. Notably, the reactive power output remains relatively steady throughout the day, with each phase consistently contributing approximately 6.00 kvar/h.

In Case B of SOP2, limited active power is available between 01:00 and 07:00. At 07:00, Phase A of bus 93 absorbs 12 kW of active power. From 08:00 to 10:00, the power absorption of Phase A increases rapidly, rising from 52.60 kW at 08:00 to a peak of 130.50 kW at 10:00. Another significant increase occurs from 11:00 to 17:00, reaching a maximum of 158.50 kW at 17:00. After 18:00, power gradually declines from 92.80 kW to just 0.40 kW by midnight. In terms of reactive power, both Phases B and C of bus 54, as well as Phase A of bus 93, show the minimal fluctuations, stabilizing at approximately 8.60 kvar. From 01:00 to 06:00, Phases B and C of bus 93 each emit 8.60 kvar per hour. Between 07:00 and 09:00, both phases maintain low levels of reactive power, averaging approximately 0.15 kvar and 0.0024 kvar, respectively. Exceptions include Phase B, which emits 8.60 kvar from 12:00 to 13:00 and from 15:00 to 17:00, and Phase C, which emits 8.60 kvar from 09:00 to 10:00 and from 16:00 to 17:00. From 22:00 to midnight, Phases B and C revert to emitting 8.60 kvar.

Several distinct trends emerge upon evaluating the power transfer capabilities and reactive power supplementation between Cases A and B in both SOP1 and SOP2 scenarios. In both situations, Case A adopts a more conservative approach to active power transfer, particularly during the initial hours, at 10:00, and from 14:00 to 18:00. By contrast, Case B exhibits superior power transmission capabilities, particularly evident in SOP1, with an average of 19.90 kW, and in SOP2 from 08:00 to 20:00, averaging 100.03 kW. In addition, Case B provides a more consistent reactive power output, with buses consistently contributing between 6.00 kvar and 8.60 kvar. This consistency highlights an improved voltage performance and enhanced reactive support in Case B. The inclusion of a reactive power source in the proposed model allows for consistently high reactive power output throughout the day, which differs from the traditional model that only achieves high reactive power output during certain time periods. Furthermore, fixed loss coefficients of the traditional model fail to accurately capture the complex quadratic relationships of losses inherent in the three-phase VSC-driven approach. This distinction in the VSC model not only reduces power losses but also enhances power transfer capabilities.

The cost analysis of SOP is presented in Table II. The network loss cost without SOP is calculated to assess the economic feasibility of SOP. In Case A, the operation cost coefficient of SOP is 0.015, reflecting the efficiency differences in power transmission between the two types of SOP.

TABLE II
COST ANALYSIS OF SOP

Case	C_{inv} ($)	C_{ope} ($)	C_{loss} ($)	Total cost ($)
Without SOP			50069.24	50069.24
Case A	1415.34	2084.40	22314.93	25814.67
Case B	1415.34	1389.60	22637.30	25442.24

Table II demonstrates that the implementation of SOP in Case B yields the greatest economic benefits. The annual total cost for Case B is $25442.24, which is $24627 less than that without SOP, representing a reduction of 49.14%. This reflects the savings from reduced power loss costs that exceed the implementation costs. In addition, compared with Case A, the total cost in Case B is reduced by $372.43. Therefore, the installation of SOP is shown to be a feasible option.

B. Comparative Analysis of Traditional and Three-phase VSC-driven BESS Models

In the traditional BESS model, the interdependence between the active and reactive power outputs is neglected, as is the relationship between the PWM-VSC control architecture and bus voltage.

Four cases (Cases 1-4) are designed to demonstrate the benefits of the three-phase VSC-driven BESS model. A three-phase VSC-driven SOP model is used to compare the BESS models.

1) Case 1: three-phase VSC-driven BESS with constant voltage E_m^{φ} (DC voltage control in [23]).

2) Case 2: three-phase VSC-driven BESS, where the charging and discharging modes (P/Q control in [23]) are the same as those in Case A in Section III-A.

3) Case 3: traditional BESS with constant voltage E_m^{φ} (DC voltage control in [23]).

4) Case 4: traditional BESS in charging and discharging modes (P/Q control in [23]).

Based on the data presented in Table III, the three-phase VSC-driven BESS model, particularly in charging and discharging modes (Case 2), stands out as the most effective configuration. It features the minimal line loss at 0.7302 MW within 24 hours and provides a reactive power supply of 0.4732 Mvar. In comparison, the charging and discharging modes in both Cases 2 and 4 consistently outperform the constant voltage control models observed in Cases 1 and 3. A noticeable reduction in active power losses is also apparent, with a significant improvement of 5.83% when transitioning from Case 4 to Case 2, and a smaller yet notable reduction of 0.68% from Case 3 to Case 1. Regarding three-phase imbalance, the three-phase VSC-driven BESS in Cases 1 and 2 shows a slight decrease in imbalance indices, measuring 7.22×10^{-2} and 7.07×10^{-2}, respectively, compared with the traditional models in Cases 3 and 4. Although Case 4 shows the lowest index of 7.01×10^{-2}, indicating some potential for improvement in traditional systems, the superior reactive power supply and efficiency benefits of the three-phase VSC-driven model in Case 2 clearly establish its dominance. Overall, these findings reinforce the idea that the three-phase VSC-driven BESS, particularly in charging and discharging modes, has the potential to optimize network performance beyond what traditional models can achieve.

TABLE III
COMPARATIVE PERFORMANCE OF TRADITIONAL AND THREE-PHASE VSC-DRIVEN BESS MODELS

Case	Line loss (MW)	Improvement rate (%)	P (MW)	Q (Mvar)	Imbalance index (10^{-2})
Case 1	0.7889	0.68	0.8136	0.4714	7.22
Case 2	0.7302	5.83	2.0000	0.4732	7.07
Case 3	0.7943		0.4871	0.0422	7.27
Case 4	0.7754		0.5000	0.0433	7.01

Figure 5 presents an analysis of the active and reactive power of the BESS in Case 2. When the load and PV curves are combined, their trends are observed to be similar to the peaks and valleys corresponding to the output of the PV source. The load curve shows peak demand in the morning and afternoon, forming the peak segments, whereas the early morning represents a load valley, creating the valley segment.

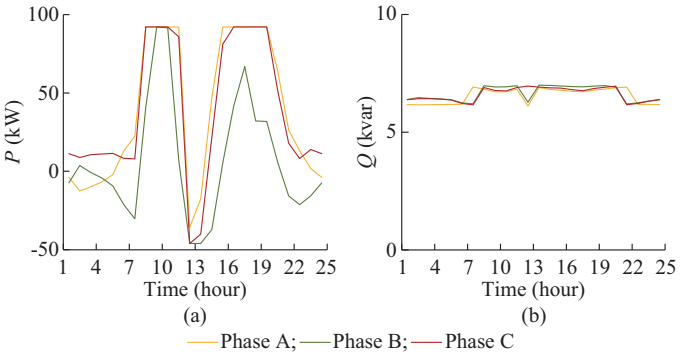

Fig. 5. Analysis of active and reactive power of BESS in Case 2. (a) Three-phase active power. (b) Three-phase reactive power.

Figure 5 clearly shows that the BESS must be charged from the DN during the early morning. As the load increases, the power output from the BESS gradually increases after absorbing power from the PV source. The period from 11:00 to 15:00 represents the peak generation time for PV, during which the BESS absorbs excess active power from the DN. After 16:00, the BESS reaches its charging limit and switches to power generation mode. After 17:00, the PV output gradually decreases to zero, and the BESS provides power to the load. After 21:00, the state of charge of the BESS decreases to approximately its initial value, completing the charging and discharging processes in a single cycle. In addition, the reactive power of the BESS, similar to that of a three-phase VSC-driven SOP, is effectively converted into a constant source, delivering stable power.

Figures 6 and 7 compare the active and reactive power in the four cases, respectively. Figure 6 indicates that in the charging and discharging modes, the novel model offers a significantly broader active power regulation range of approximately −50 kW to 100 kW, compared with the much narrower range of the traditional model of −6 kW to 12 kW. This enhanced capability makes the proposed model a more adaptable solution for meeting power regulation demands within the DN. In addition, the three-phase VSC-driven model operating in constant value mode can deliver four times the active power of the traditional model, effectively demonstrating the energy supply capacity of the BESS to the DN. Moreover, the BESS in charging and discharging modes adjusts according to load fluctuations, leading to greater energy savings than those in constant value mode.

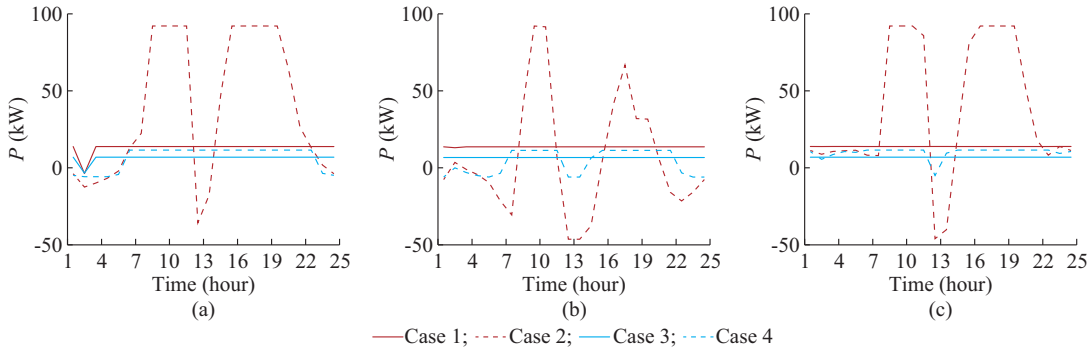

Fig. 6. Active power of BESS in four cases. (a) Phase A. (b) Phase B. (c) Phase C.

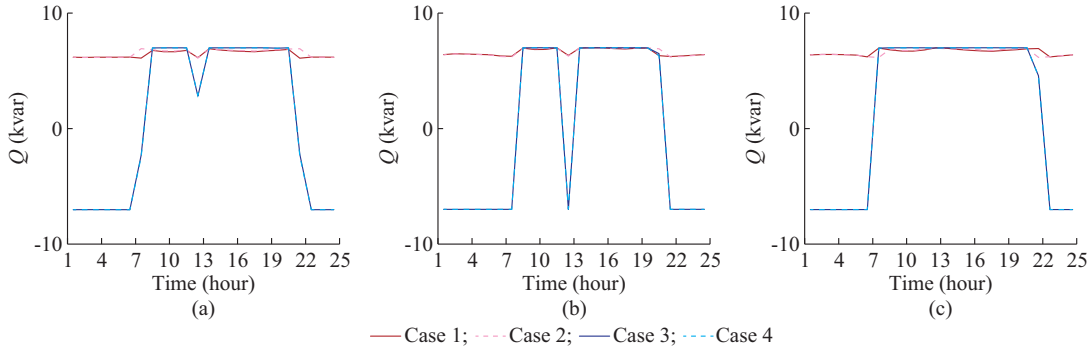

Fig. 7. Reactive power of BESS in four cases. (a) Phase A. (b) Phase B. (c) Phase C.

From Fig. 7, we can deduce that the reactive power output of the three-phase VSC-driven model remains relatively stable. By contrast, the reactive power of the traditional model stabilizes only briefly and requires power absorption from the DN during the early morning and nighttime hours. Compared with the conventional BESS, the three-phase VSC-driven BESS functions as an equivalent power source, better supplying reactive power to the load and improving the reactive

power level of the DN.

C. Voltage Performance

As Fig. 8 shows, bus voltages are analyzed over a 24-hour period. With the regulation of BESS and SOP, the voltage remains generally stable within the specified range. During peak load hours, a slight reduction in bus voltage is observed, but it does not fall below the lower limit. When the bus voltage decreases, the modulation factor increases accordingly to restore the voltage to its normal level, remaining relatively constant when the voltage is stable. However, as this modulation factor is influenced not only by voltage but also by reactive power, significant fluctuations occur in Phases B and C of bus 93 to coordinate changes in reactive power, as illustrated in Fig. 8(c).

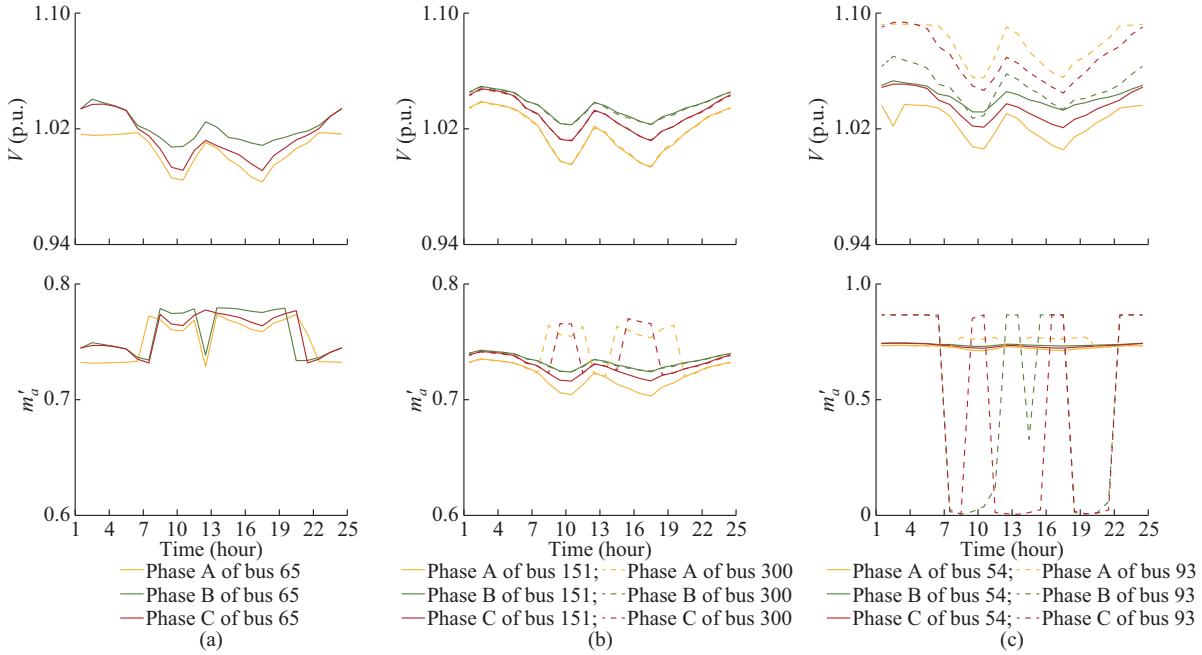

Fig. 8. Three-phase voltage and amplitude modulation index of VSC. (a) BESS. (b) SOP1. (c) SOP2.

D. Evaluation of Impact of PSD Installations

The impact of PSD installations on network management is evaluated by illustrating the relationship between the number of installed PSDs and the subsequent improvements in power losses and three-phase balance, as shown in Table IV.

TABLE IV
IMPACT OF PSD INSTALLATIONS ON NETWORK MANAGEMENT

Number of PSD installations	Bus number	Power loss (MW)	Improvement rate (%)	Imbalance Index (10^{-2})
0		0.7302		7.07
2	48, 76	0.7025	3.79	6.48
4	47, 48, 49, 76	0.7021	3.85	6.41
6	7, 47, 48, 49, 65, 76	0.7000	4.14	6.36

An increase in the number of PSD installations is associated with a noticeable reduction in line power losses. As Table IV shows, without any PSDs, the line loss is 0.7302 MW, accompanied by a three-phase imbalance index of 7.07×10^{-2}. The addition of two PSDs on buses 48 and 76 results in a 3.79% improvement in power losses and a significant reduction in the imbalance index to 6.48×10^{-2}. Increasing the count to four PSDs sited on buses 47, 48, 49, and 76 yields a slightly better 3.85% reduction in power losses, with an imbalance index of 6.41×10^{-2}. Notably, installing six PSDs across buses 7, 47, 48, 49, 65, and 76 achieves a 4.14% decrease in power losses, further improving the balance to an index of 6.36×10^{-2}. Nevertheless, the incremental advantages in line losses tend to diminish as the number of PSDs increases. This observation highlights the importance of carefully weighing economic and efficiency trade-offs when planning PSD installations.

IV. CONCLUSION

This paper clearly highlights the advantages of integrating VSC technology into SOP models. The proposed VSC-driven model for SOPs significantly outperforms traditional SOP, reducing line losses from 0.7382 MW to 0.7302 MW over 24 hours and improving the three-phase imbalance index from 8.58×10^{-2} to 7.07×10^{-2}. These metrics demonstrate the enhanced efficiency and balance of the proposed model. In addition, the enhancements in both active and reactive power indicate the advantages of the proposed model in power quality management.

This paper also provides a valuable comparison of proposed VSC-driven and traditional models for BESSs, underscoring the transformative benefits particularly with PSD installations. This combination enhances the adaptability of BESS with advanced VSC technologies, resulting in improved power quality and three-phase balance. By utilizing a

symmetrical SDP and convex relaxation, BD is employed to solve the mixed-integer programming for three-phase optimal power flow, enabling the determination of the transformer tap ratio and phase setting of the PSD. This paper not only clarifies the advantages of using the three-phase devices but also proposes an innovative approach for system optimization, establishing a solid foundation for future research aimed at enhancing the accuracy and efficiency of DNs.

REFERENCES

[1] D. Fan, H. Wang, F. Wang *et al*., "Three-phase imbalance governance method for distribution network based on big data analysis," in *Proceedings of 2021 IEEE 4th International Conference on Computing, Power and Communication Technologies*, Kuala Lumpur, Malaysia, Sept. 2021, pp. 1-6.

[2] C. Vidal, L. Tarisciotti, M. Díaz *et al*., "Application of a single-phase matrix converter for electric vehicle charging," in *Proceedings of 2022 IEEE Biennial Congress of Argentina*, San Juan, Argentina, Sept. 2022, pp. 1-7.

[3] S. B. Kjaer, J. K. Pedersen, and F. Blaabjerg, "A review of single-phase grid-connected inverters for photovoltaic modules," *IEEE Transactions on Industry Applications*, vol. 41, no. 5, pp. 1292-1306, Sept.-Oct.2005.

[4] X. Zeng, H. Zhai, M. Wang *et al*., "A system optimization method for mitigating three-phase imbalance in distribution network," *International Journal of Electrical Power Energy Systems*, vol. 113, pp. 618-633, Dec. 2019.

[5] S. Soltani, M. Rashidinejad, and A. Abdollahi, "Dynamic phase balancing in the smart distribution networks," *International Journal of Electrical Power & Energy Systems*, vol. 93, pp. 374-383, Dec. 2017.

[6] F. Ni, J. Q. Liu, F. Wei *et al*., "Phase identification in distribution systems by data mining methods," in *Proceedings of 2017 IEEE Conference on Energy Internet and Energy System Integration*, Beijing, China, Nov. 2017, pp. 1-6.

[7] S. Liu, X. Cui, Z. Lin *et al*., "Practical method for mitigating three-phase unbalance based on data-driven user phase identification," *IEEE Transactions on Power Systems*, vol. 35, no. 2, pp. 1653-1656, Mar. 2020.

[8] O. Homaee, A. Najafi, M. Dehghanian *et al*., "A practical approach for distribution network load balancing by optimal re-phasing of single phase customers using discrete genetic algorithm," *International Transactions on Electrical Energy Systems*, vol. 29, no. 5, p. e2834, May 2019.

[9] X. Zeng, H. Zhai, M. Wang *et al*., "A system optimization method for mitigating three-phase imbalance in distribution network," *International Journal of Electrical Power & Energy Systems*, vol. 113, pp. 618-633, Dec. 2019.

[10] S. Liu, Z. Lin, J. Li *et al*., "Bi-level optimal placement model of phase switch devices for mitigating three-phase unbalance in low-voltage areas," *IEEE Transactions on Power Systems*, vol. 37, no. 4, pp. 3149-3152, Jul. 2022.

[11] F. Liang, J. Ni, H. Zhu *et al*., "Optimal phase switch device placement scheme for low voltage distribution network considering load and renewable energy uncertainty," in *Proceedings of 2022 Asia Power and Electrical Technology Conference*, Shanghai, China, Nov. 2022, pp. 157-160.

[12] C. E. Free and C. S. Aitchison, *Switches and Phase Shifters*. Hoboken: John Wiley & Sons, 2022, pp. 267-299.

[13] B. Liu, F. Geth, N. Mahdavi *et al*., "Load balancing in low-voltage distribution networks via optimizing residential phase connections," in *Proceedings of 2021 IEEE PES Innovative Smart Grid Technologies – Asia*, Brisbane, Australia, Dec. 2021, pp. 1-5.

[14] S. H. Soltani, M. Rashidinejad, and A. Abdollahi, "Dynamic phase balancing in the smart distribution networks," *International Journal of Electrical Power & Energy Systems*, vol. 93, pp. 374-383, Dec. 2017.

[15] B. Liu, K. Meng, Z. Y. Dong *et al*., "Unbalance mitigation via phase-switching device and static var compensator in low-voltage distribution network," *IEEE Transactions on Power Systems*, vol. 35, no. 6, pp. 4856-4869, May 2020.

[16] A. Nakadomari, R. Shigenobu, and T. Senjyu, "Optimal control and placement of step voltage regulator for voltage unbalance improvement and loss minimization in distribution system," in *Proceedings of 2020 IEEE Region 10 Conference*, Osaka, Japan, Nov. 2020, pp. 1013-1018.

[17] M. Chamana and B. H. Chowdhury, "Optimal voltage regulation of distribution networks with cascaded voltage regulators in the presence of high PV penetration," *IEEE Transactions on Sustainable Energy*, vol. 9, no. 3, pp. 1427-1436, Jan. 2018.

[18] J. Wang, N. Zhou, Y. Ran *et al*., "Optimal operation of active distribution network involving the unbalance and harmonic compensation of converter," *IEEE Transactions on Smart Grid*, vol. 10, no. 5, pp. 5360-5373, Sept. 2019.

[19] M. Yao, I. A. Hiskens, and J. L. Mathieu, "Mitigating voltage unbalance using distributed solar photovoltaic inverters," *IEEE Transactions on Power Systems*, vol. 36, no. 3, pp. 2642-2651, May 2021.

[20] J. Li, Z. Hai, Z. Shuai *et al*., "Coordinated current and voltage unbalance mitigation in networked microgrids with aggregated PV systems," *IEEE Transactions on Power Systems*, vol. 38, no. 1, pp. 968-971, Jan. 2023.

[21] T. W. Tsai, Y. Li, C. Yang *et al*., "Per-phase active power distribution strategy for three-phase grid-tied inverters under unbalanced conditions without DC sources," *IEEE Journal of Emerging and Selected Topics in Power Electronics*, vol. 9, no. 6, pp. 6624-6636, Dec. 2021.

[22] A. Garcés, J. C. Castaño, and M. A. Rios, "Phase balancing in power distribution grids: a genetic algorithm with a group-based codification," in *Handbook of Optimization in Electric Power Distribution Systems*, Cham: Springer, pp. 325-342, 2020.

[23] X. Jiang, Y. Zhou, W. Ming *et al*., "An overview of soft open points in electricity distribution networks," *IEEE Transactions on Smart Grid*, vol. 13, no. 3, pp. 1899-1910, May 2022.

[24] A. Tao, N. Zhou, Y. Chi *et al*., "Multi-stage coordinated robust optimization for soft open point allocation in active distribution networks with PV," *Journal of Modern Power Systems and Clean Energy*, vol. 11, no. 5, pp. 1553-1563, Sept. 2023.

[25] Z. Li, Z. Tang, W. Chao *et al*., "Multi-objective supply restoration in active distribution networks with soft open points," in *Proceedings of 2018 2nd IEEE Conference on Energy Internet and Energy System Integration*, Beijing, China, Oct. 2018, pp. 1-5.

[26] Z. Liu and L. Wang, "A robust strategy for leveraging soft open points to mitigate load altering attacks," *IEEE Transactions on Smart Grid*, vol. 13, no. 2, pp. 1555-1569, Dec. 2021.

[27] H. Ji, C. Wang, P. Li *et al*., "Robust operation of soft open points in active distribution networks with high penetration of photovoltaic integration," *IEEE Transactions on Sustainable Energy*, vol. 10, no. 1, pp. 280-289, Jan. 2019.

[28] C. Lou, J. Yang, T. Li *et al*., "New phase-changing soft open point and impacts on optimising unbalanced power distribution networks," *IET Generation*, *Transmission & Distribution*, vol. 14, no. 23, pp. 5685-5696, Dec. 2020.

[29] C. Lou, J. Yang, E. Vega-Fuentes *et al*., "Multi-terminal phase-changing soft open point SDP modeling for imbalance mitigation in active distribution networks," *International Journal of Electrical Power & Energy Systems*, vol. 142, p. 108228, Nov. 2022.

[30] X. Cui, G. Ruan, F. Vallée *et al*., "A two-level coordination strategy for distribution network balancing," *IEEE Transactions on Smart Grid*, vol. 15, no. 1, pp. 529-544, Jan. 2024.

[31] L. Min, J. Yang, C. Lou *et al*., "Phase-changing control for three-phase four-wire back-to-back VSC based soft open points," in *Proceedings of 11th International Conference on Renewable Power Generation*, London, UK, Sept. 2022, pp. 110-114.

[32] T. Wu, Y. Zhang, and X. Tang, "A VSC-based BESS model for multi-objective OPF using mixed integer SOCP," *IEEE Transactions on Power Systems*, vol. 34, no. 4, pp. 2541-2552, Jul. 2019.

[33] T. Wu, C. Zhao, and Y. Zhang, "Distributed AC-DC optimal power dispatch of VSC-based energy routers in smart microgrids," *IEEE Transactions on Power Systems*, vol. 36, no. 5, pp. 4457-4470, Sept. 2021.

[34] Z. Wang, D. S. Kirschen, and B. Zhang. (2017, Dec.). Accurate semi-definite programming models for optimal power flow in distribution systems. [Online]. Available: https://arxiv.org/abs/1711.07853v2

[35] G. C. Paap, "Symmetrical components in the time domain and their application to power network calculations," *IEEE Transactions on Power Systems*, vol. 15, no. 2, pp. 522-528, May 2000.

[36] P. M. Anderson, *Analysis of Faulted Power Systems*. Hoboken: John Wiley & Sons, 1995.

[37] M. Abdel-Akher and K. M. Nor, "Fault analysis of multiphase distribution systems using symmetrical components," *IEEE Transactions on Power Delivery*, vol. 25, no. 4, pp. 2931-2939, Oct. 2010.

[38] B. Kazemtabrizi and E. Acha, "An advanced STATCOM model for optimal power flows using Newton's method," *IEEE Transactions on Power Systems*, vol. 29, no. 2, pp. 514-525, Mar. 2014.

[39] I. Alsaleh, L. Fan and M. Ma, "Mixed-integer SDP relaxation-based

volt/var optimization for unbalanced distribution systems," in *Proceedings of 2019 IEEE PES General Meeting*, Atlanta, USA, Aug. 2019, pp. 1-5.
[40] I. Alsaleh and L. Fan, "Multi-time co-optimization of voltage regulators and photovoltaics in unbalanced distribution systems," *IEEE Transactions on Sustainable Energy*, vol. 12, no. 1, pp. 482-491, Jan. 2021.
[41] R. Rahmaniani, T. G. Crainic, M. Gendreau *et al*., "The Benders decomposition algorithm: a literature review," *European Journal of Operational Research*, vol. 259, no. 3, pp. 801-817, Jun. 2017.
[42] A. M. Geoffrion, "Generalized Benders decomposition," *Journal of Optimization Theory and Applications*, vol. 10, no. 4, pp. 237-260, Oct. 1972.
[43] M. Paredes, L. S. A. Martins, S. Soares *et al*., "Benders' decomposition of the unit commitment problem with semidefinite relaxation of AC power flow constraints," *Electric Power Systems Research*, vol. 192, p. 106965, Mar. 2021.
[44] A. Soares, A. Street, T. Andrade *et al*., "An integrated progressive hedging and benders decomposition with multiple master method to solve the Brazilian generation expansion problem," *IEEE Transactions on Power Systems*, vol. 37, no. 5, pp. 4017-4027, Sept. 2022.
[45] B. Zhang, L. Zhang, W. Tang *et al*., "Optimal planning of hybrid AC/DC low-voltage distribution networks considering DC conversion of three-phase four-wire low-voltage AC systems," *Journal of Modern Power Systems and Clean Energy*, vol. 12, no. 1, pp. 141-153, Jan. 2024.
[46] P. Li, H. Ji, C. Wang *et al*., "Coordinated control method of voltage and reactive power for active distribution networks based on soft open point," *IEEE Transactions on Sustainable Energy*, vol. 8, no. 4, pp. 1430-1442, Oct. 2017.
[47] C. Wang, G. Song, P. Li *et al*., "Optimal siting and sizing of soft open points in active electrical distribution networks," *Applied Energy*, vol. 189, pp. 301-309, Mar. 2017.
[48] J. Lofberg, "YALMIP: a toolbox for modeling and optimization in MATLAB," in *Proceedings of 2004 IEEE International Conference on Robotics and Automation*, Taipei, China, Sept. 2004, pp. 284-289.
[49] P. Li, H. Ji, C. Wang *et al*., "Optimal operation of soft open points in active distribution networks under three-phase unbalanced conditions," *IEEE Transactions on Smart Grid*, vol. 10, no. 1, pp. 380-391, Jan. 2019.

Chengwei Lou received the B.S. and the M.E. degrees in electrical engineering and automation from China Agricultural University, Beijing, China, in 2016 and 2019, respectively, and the Ph.D. degree in electrical engineering from University of Glasgow, Glasgow, UK, in 2022. He is currently an Associate Professor with College of Information and Electrical Engineering, China Agricultural University. His current research interests include power distribution system modelling and optimization.

Ran Zhao is currently working toward the M.E. degree in electrical engineering from China Agricultural University, Beijing, China. Her main research interests include resilience enhancement in hybrid AC/DC distribution network and active distribution network.

Hangxing Zhang is currently working toward the M.E. degree in electrical engineering from China Agricultural University, Beijing, China. His main research interests include application of Benders decomposition algorithm and electric vehicle.

Lu Zhang received the B.S. degree in electrical engineering and the Ph.D. degree in agricultural electrification and automation from China Agricultural University, Beijing, China, in 2011 and 2016, respectively. From 2017 to 2019, he was a Postdoc with the Department of Electrical Engineering, Tsinghua University, Beijing, China. He is currently a Professor with the College of Information and Electrical Engineering, China Agricultural University. His main research interests include hybrid AC/DC distribution network, renewable energy generation, and active distribution network.

Wei Tang received the B.S. degree in electrical engineering from Huazhong University of Science and Technology, Wuhan, China, in 1992, and the Ph.D. degree in electrical engineering from Harbin Institute of Technology, Harbin, China, in 1998. From 1998 to 2000, she was a Postdoc with Harbin Engineering University, Harbin, China. She is currently a Professor with the College of Information and Electrical Engineering, China Agricultural University, Beijing, China. Her research interests include economic and security operation of distribution network, distributed generation, and active distribution network.

Jin Yang received the Ph.D. degree from University of Glasgow, Glasgow, UK, in 2011. He is currently a Reader in James Watt School of Engineering, University of Glasgow. His research interests include flexible and innovative operational technology of renewable distributed energy resource, and its impacts on distribution network.

Linjuan Zhang is currently working at State Grid Henan Economic Research Institute, Zhengzhou, China. Her research interests include orderly charging of electric vehicle and charging network.